Journal of Solid State Chemistry 182 (2009) 767–777

Contents lists available at ScienceDirect

Journal of Solid State Chemistry

journal homepage: www.elsevier.com/locate/jssc

High-pressure behavior of the ternary bismuth oxides $Bi_2Al_4O_9$, $Bi_2Ga_4O_9$ and $Bi_2Mn_4O_{10}$

Laura López-de-la-Torre [a], Alexandra Friedrich [a,*], Erick A. Juarez-Arellano [a], Björn Winkler [a], Dan J. Wilson [a], Lkhamsuren Bayarjargal [a], Michael Hanfland [b], Manfred Burianek [c], Manfred Mühlberg [c], Hartmut Schneider [c]

[a] Institut für Geowissenschaften, Abt. Kristallographie, Goethe-Universität Frankfurt, Altenhöferallee 1, D-60438 Frankfurt am Main, Germany
[b] ESRF, BP 220, F-38043, Grenoble CEDEX, France
[c] Institut für Kristallographie, Universität zu Köln, Zülpicherstrasse 49b, D-50674 Cologne, Germany

ARTICLE INFO

Article history:
Received 16 October 2008
Received in revised form
12 December 2008
Accepted 17 December 2008
Available online 7 January 2009

Keywords:
High pressure
Powder X-ray diffraction
Density functional theory
Phase transition
Bismuth oxides

ABSTRACT

The high-pressure behavior of $Bi_2Al_4O_9$, $Bi_2Mn_4O_{10}$ and $Bi_2Ga_4O_9$ was investigated by *in situ* powder synchrotron X-ray diffraction. Pressures up to 35 GPa were generated using the diamond anvil cell technique. Complementary data of the pressure dependence of $Bi_2Ga_4O_9$ were obtained by density functional theory-based model calculations. $Bi_2Al_4O_9$ and $Bi_2Mn_4O_{10}$ are structurally stable to the highest pressures obtained. In contrast, a reversible phase transition is observed in $Bi_2Ga_4O_9$ at approximately 16 GPa. A fit of a 3rd-order Birch–Murnaghan equation of state to the $p-V$ data results in $V_0 = 356.93(9)$ Å^3, $B_0 = 122(2)$ GPa and $B' = 4.9(3)$ for $Bi_2Al_4O_9$; $V_0 = 372.27(1)$ Å^3, $B_0 = 138(2)$ GPa and $B' = 4.2(2)$ for $Bi_2Mn_4O_{10}$; and $V_0 = 388.63(3)$ Å^3, $B_0 = 102(8)$ GPa and $B' = 3.8(2)$ for $Bi_2Ga_4O_9$. The most compressible axis is the *a* axis for all the compounds. This behavior can be rationalized in terms of the inflexible polyhedra connections parallel to the *b* and *c* axes.

1. Introduction

Compounds of the composition $Bi_2M_4O_9$ ($M = Al^{3+}$, Ga^{3+}, Fe^{3+}), $Bi_2Z_2M_2O_{10}$ ($Z = Mn^{4+}$, $M = Mn^{3+}$), and the respective solid solutions, belong to the family of sillimanite- and mullite-type crystal structures [1,2]. These materials exhibit interesting properties, for instance photoluminescence [3–5] or oxygen ionic conductivity [6], especially if part of the Bi^{3+} is replaced by twofold charged cations, like Sr^{2+}, Ca^{2+}, and Ba^{2+} [7]. Hence, they are potential candidates for applications such as electrolytes of solid oxide fuel cells, oxygen sensors, and gas separation membranes [7,8]. On the other hand, the $Bi_2Mn_4O_{10}$ compound has interesting magnetic properties [1].

This structural family is characterized by chains of edge-sharing octahedra extending parallel to the *c* axis. Alternating along [110], half of the octahedral chains are rotated clockwise, the other half counterclockwise. In sillimanite (Al_2SiO_5, space group *Pbnm*, Fig. 1) and mullites *sensu stricto* ($Al_{4+2x}Si_{2-2x}O_{10-x}$, normally $0.2 \leqslant x \leqslant 0.5$, space group *Pbam*), the octahedra are occupied by aluminum. In sillimanite, the octahedral chains are cross-linked via double chains of corner-sharing tetrahedral groups extending parallel to the *c* axis, with the tetrahedra alternately occupied by silicon and aluminum (Fig. 1) [9]. The crystal structures of mullites can be derived from that of sillimanite with part of the oxygen atoms, which bridge the tetrahedral double chains in sillimanite, missing. The number of oxygen vacancies refers to the index of the general formula $Al_{4+2x}Si_{2-2x}O_{10-x}$. It is accompanied by substitution of Al^{3+} for Si^{4+} and formation of tetrahedral triclusters [1].

The crystal structure of the $Bi_2M_4O_9$ compounds, shown in Fig. 1, is orthorhombic with space group *Pbam* [8]. The unit cell contains two formula units. Half of the M^{3+} ions are tetrahedrally coordinated, the other half is octahedrally coordinated. The bonding environment of the Bi^{3+} ion is strongly anisotropic with three strong and one weaker Bi–O bonds on one side, and the lone electron pair on the other [8]. Similar to the sillimanite and mullite structures, chains of edge-sharing MO_6 octahedra run parallel to the *c*-axis (Fig. 1). The octahedral chains are linked via pairs of corner-sharing MO_4 tetrahedra, forming M_2O_7 dimers, and via highly asymmetric BiO_4 groups [2]. The M_2O_7 dimers are arranged in *ab* planes and alternate with planes of BiO_4 groups along the *c* axis. Hence, the central oxygen atoms of the M_2O_7 dimers alternate with vacant sites, which are created by the orientation of the lone electron pairs of two facing Bi^{3+} ions pointing towards these sites (Fig. 2) [8].

The structure of $Bi_2Z_2M_2O_{10}$ ($Z = Mn^{4+}$, $M = Mn^{3+}$), shown in Fig. 1, is closely related to the $Bi_2M_4O_9$ structure, also crystallizing in space group *Pbam* [11], and with chains of edge-sharing ZO_6

* Corresponding author. Fax: +49 69 798 40109.
E-mail address: friedrich@kristall.uni-frankfurt.de (A. Friedrich).

0022-4596/$ - see front matter © 2009 Elsevier Inc. All rights reserved.
doi:10.1016/j.jssc.2008.12.019

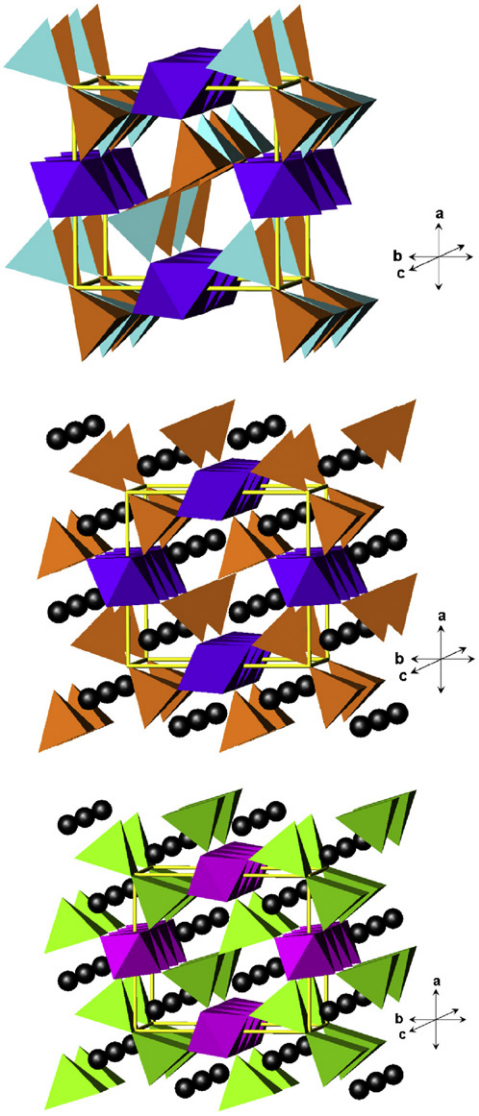

Fig. 1. (Color online) Crystal structures of sillimanite, Al_2SiO_5 [10] (top), $Bi_2Al_4O_9$ [8] (middle), and $Bi_2Mn_4O_{10}$ [11] (bottom) at ambient conditions. Dark gray (violet) octahedra represent AlO_6 groups (top and center) or MnO_6 groups (magenta, bottom). Medium gray (orange) tetrahedra represent AlO_4 groups (top and center), light gray (blue) tetrahedra SiO_4 groups (top), while light gray (green) square pyramids represent MnO_5 groups (bottom). Bismuth atoms are drawn as black balls. The unit cell of sillimanite is shifted by −0.5, 0, 0 for comparison.

octahedra running parallel to the *c* axis. Groups of edge-sharing MO_5 square pyramids in *ab* planes alternate with *ab* planes of distorted BiO_6 polyhedra. While in $Bi_2M_4O_9$ the bridging oxygen ion of the M_2O_7 dimers is located at $0, 0, \frac{1}{2}$, in $Bi_2Z_2M_2O_{10}$ two MO_5 square pyramids share an edge along the *c* axis via two oxygen atoms situated at $0, 0, \pm 0.281$ (Fig. 3). The main difference between the $Bi_2Mn_4O_{10}$ structure and the $Bi_2M_4O_9$ structure is due to the 'addition of' oxygen, which participates in the fivefold square-pyramidal coordination of the Mn^{3+} [11,12]. The coordination of bismuth by oxygen consists of three short Bi−O bonds, mutually orthogonal, and three longer Bi−O bonds [11].

Although many studies have been performed on these materials (e.g. [2–5,7,8,11–14]) their high-pressure behavior has not yet been investigated. The existence of a Bi^{3+} lone electron pair, which is assumed to be highly compressible, makes these structures especially interesting for high-pressure investigations. Compressing the structure and hence the localized lone electron pair might lead to a symmetrization of the distorted Bi^{3+} environment and hence to a phase transition [15]. In this study, we have performed quantum-mechanical calculations based on density functional theory (DFT) on the high-pressure behavior of $Bi_2Ga_4O_9$. As the DFT-results indicated changes of the structural compression mechanism of $Bi_2Ga_4O_9$ at high pressure, we have subsequentially investigated $Bi_2Ga_4O_9$ and the structurally related $Bi_2Al_4O_9$ and $Bi_2Mn_4O_{10}$ by *in situ* powder synchrotron X-ray diffraction using the diamond anvil cell technique to generate pressures up to 29 GPa for $Bi_2Al_4O_9$, and up to 35 GPa for $Bi_2Mn_4O_{10}$ and $Bi_2Ga_4O_9$. Here, we present a comparative analysis of the compressibilities and high-pressure phase stabilities of these compounds.

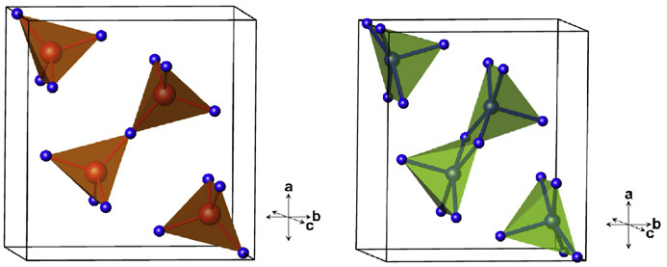

Fig. 3. (Color online) Comparison of the M_2O_7 (M = Al, Ga) dimers (corner-sharing tetrahedra, orange) with the Mn_2O_8 dimers (edge-sharing square pyramids, magenta) in (left) $Bi_2M_4O_9$ (M = Al, Ga) and (right) $Bi_2Mn_4O_{10}$.

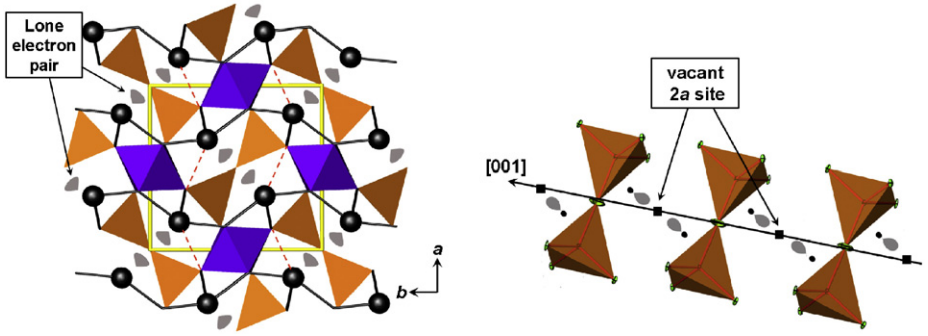

Fig. 2. (Color online) Left: localization of the lone electron pair in the crystal structure of $Bi_2M_4O_9$, M = Al, Ga. Right: along the *c* axis the central oxygen atoms of the M_2O_7 dimers of the $Bi_2M_4O_9$ structure alternate with vacant sites, which are created by the orientation of the lone electron pairs of two facing Bi^{3+} ions pointing towards these sites. MO_4 tetrahedra are drawn in light gray (orange), MO_6 octahedra in dark gray (violet). Black balls represent bismuth atoms. The strong Bi–O bonds are drawn as black lines and show the connectivity along the *b* axis. Additional weak Bi–O bonds exist along the gray (red) dotted lines nearly parallel to the *a* axis.

2. Experimental methods

2.1. Syntheses

Single crystals of the compositions $Bi_2M_4O_9$ ($M = Al^{3+}$, Ga^{3+}) and $Bi_2Z_2M_2O_{10}$ ($Z = Mn^{4+}$, $M = Mn^{3+}$) with mullite-type crystal structure have been melt-grown by means of the top-seeded solution growth (TSSG) technique. The crystal growth of these phases is difficult as it is controlled by incongruent melting with steep liquidus curves in the growth range between 1343 and 1123 K, depending on the phase composition. Furthermore, according to the conditions constrained by the phase diagram, the volume ratio between as-grown crystals and starting melts is much less than unity ($Bi_2Ga_4O_9$: 26%, $Bi_2Al_4O_9$: 6%, $Bi_2Mn_4O_{10}$: 4%). High purity Bi_2O_3, Al_2O_3, and Mn_2O_3 were used for single crystal syntheses. Experiments were carried out in Pt crucibles (volume: 60–100 ml) in resistance-heated tube furnaces with KANTHAL A1 heating elements and were monitored by constantly weighing the crucibles. To avoid melt supercooling and spontaneous nucleation, cooling rates were kept very low in each case (3 K/d). Well-shaped, homogeneous and nearly inclusion-free crystals have been obtained: $Bi_2Ga_4O_9$ ($35 \times 35 \times 10\,mm^3$, pale-yellow and transparent), $Bi_2Al_4O_9$ ($5 \times 3 \times 2\,mm^3$, brown and transparent) and $Bi_2Mn_4O_{10}$ ($10 \times 10 \times 5\,mm^3$, black and opaque).

Powder samples were obtained from grinding small pieces of single crystals. In the case of $Bi_2Ga_4O_9$ the same single crystal was used as for the resonant ultrasound spectroscopic study [2].

2.2. Powder X-ray diffraction measurements

The $Bi_2Al_4O_9$, $Bi_2Mn_4O_{10}$ and $Bi_2Ga_4O_9$ powder samples were studied using synchrotron X-ray radiation at the ESRF. To reach pressures up to 35 GPa, a Le Toullec diamond anvil cell with a gas-driven membrane for pressure generation was used [16]. The pressure-transmitting medium was neon for $Bi_2Mn_4O_{10}$ and helium for $Bi_2Al_4O_9$ and $Bi_2Ga_4O_9$. Both gases were loaded using an autoclave. Holes of about 150 μm in diameter, serving as sample chambers, were drilled through steel gaskets (pre-indented to a thickness of 45 μm) with a spark-eroding drilling machine. Before and after each exposure, pressure was determined by the laser-induced ruby-fluorescence technique [17]. *In situ* high-pressure synchrotron X-ray powder diffraction data were collected at the ID09A high-pressure station with a wavelength of 0.3729 Å using a MAR345 online image-plate scanner. The sample-to-detector distance of 365 mm allowed data collection up to $2\theta = 24^\circ$ giving a maximum $\sin\theta/\lambda$ of 0.558 $Å^{-1}$.

The processing and integration of the diffraction images were performed using the program FIT2D [18], manually masking single diffraction spots from the sample and pressure medium and excluding them from the integration. The DATLAB [19] program was used to extract the background from the integrated powder diffraction patterns. Cell parameters were refined using the Le Bail method by means of the program general structure analysis system (GSAS) [20]. The starting values of the lattice parameters used for the refinements were taken from Abrahams et al. for $Bi_2Al_4O_9$ [8], from Niizeki et al. for $Bi_2Mn_4O_{10}$ [11], and from Mueller-Buschbaum et al. for $Bi_2Ga_4O_9$ [21]. Representative examples of the Le Bail fits for low and high pressures and their respective difference plots are shown in Figs. 4, 5 and 6 for $Bi_2Al_4O_9$, $Bi_2Mn_4O_{10}$ and $Bi_2Ga_4O_9$, respectively. The resolution of the $Bi_2Mn_4O_9$ data, and hence the quality of the refinements, decreases above ≈ 16 GPa as can be inferred from the peak broadening (Fig. 5). This seems to be due to the use of neon as the pressure medium, which behaves less hydrostatically than helium at very high pressures.

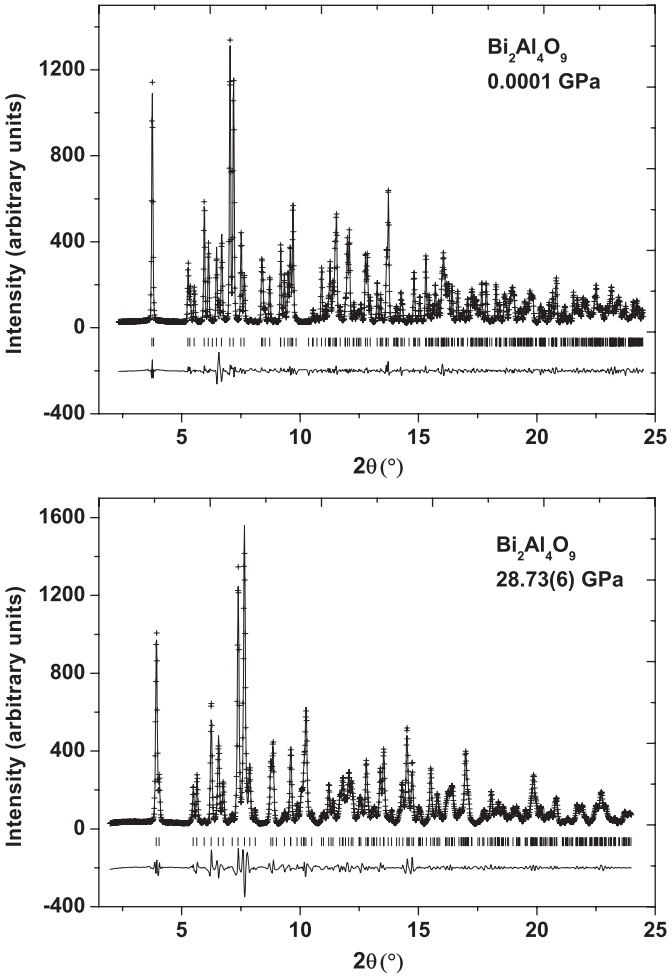

Fig. 4. X-ray powder diffraction patterns for $Bi_2Al_4O_9$ at 0.0001 and 28.73 GPa. Symbols (+) represent experimental values. The result of the Le Bail fit is shown by the continuous line through the data points. The difference between the Le Bail fit and the experimental values is represented by the line at the bottom of the plots, which has been shifted by −200 units. Vertical bars show the positions of the allowed Bragg reflections of $Bi_2Al_4O_9$.

3. Data analysis

Equation-of-state (EOS) parameters V_0 (unit cell volume at ambient pressure), K_0 (isothermal bulk modulus) and K' (pressure derivative of K) of $Bi_2Al_4O_9$, $Bi_2Mn_4O_{10}$ and $Bi_2Ga_4O_9$ were determined by a least-squares fit to a Birch–Murnaghan EOS or to a Vinet EOS using the program EOS-FIT [22]. The pressure–volume ($p-V$) data were weighted with the experimental errors of the pressures and volumes. Furthermore, the pressure–volume data were transformed into the Eulerian strain f ($f = 0.5[(V_0/V)^{2/3} - 1]$) as a function of the normalized pressure F ($F = p/[3f(1+2f)^{5/2}]$), in order to visualize complex trends which are not directly apparent from the $p-V$ plots. If $F(f) =$ constant then $K' = 4$. An inclined straight line with positive or negative slope implies $K' > 4$ or $K' < 4$, respectively. In all cases, the intercept on the F axis is the value of K_0 [23]. A curvature of the plot either suggests an EOS of higher order, a change of the compression mechanism or a structural phase transition.

As the EOS fits to the lattice parameters partly resulted in very high or negative values for K', which represents unphysical behavior, the Eulerian finite-strain analysis was extended to obtain the compression behavior of the unit cell axes. In an orthogonal system the calculation of the Eulerian strain f is

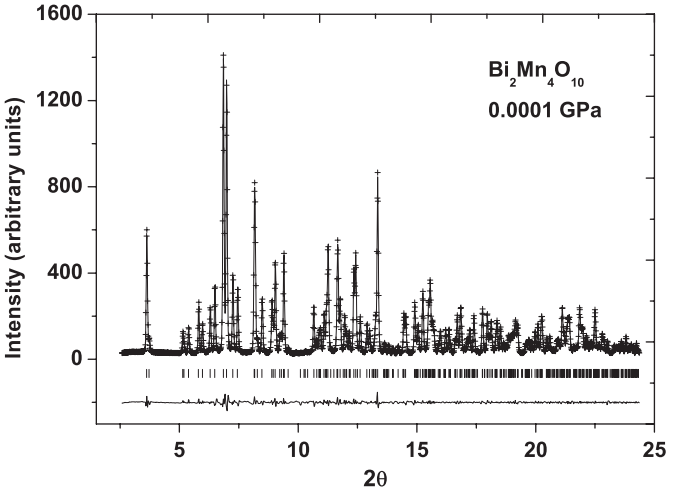

Fig. 5. X-ray powder diffraction patterns for $Bi_2Mn_4O_{10}$ at 0.0001 and 34.38 GPa. Symbols (+) represent experimental values. The result of the Le Bail fit is shown by the continuous line through the data points. The difference between the Le Bail fit and the experimental values is represented by the line at the bottom of the plots, which has been shifted by −200 (top) and −300 units (bottom). Vertical bars show the positions of the allowed Bragg reflections of $Bi_2Mn_4O_{10}$ and of neon (top row at 34.38 GPa).

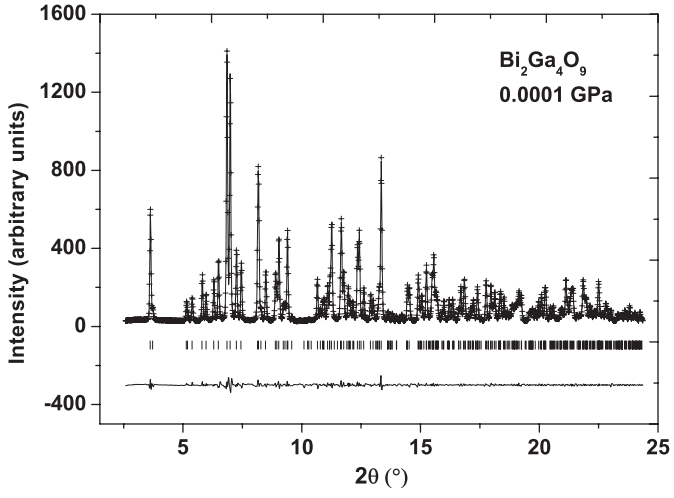

Fig. 6. X-ray powder diffraction patterns for $Bi_2Ga_4O_9$ at 0.0001 and 34.89 GPa. Symbols (+) represent experimental values. The result of the Le Bail fit is shown by the continuous line through the data points. The difference between the Le Bail fit and the experimental values is represented by the line at the bottom of the plots, which has been shifted by −300 units. Vertical bars show the positions of the allowed Bragg reflections of $Bi_2Ga_4O_9$.

similar for the cell parameters as for the $p-V$ data, while F has to be divided by a factor of three.

4. Computational details

The quantum mechanical calculations performed here were based on DFT. While DFT itself is exact, practical calculations employing the Kohn Sham formalism require an approximation for the treatment of the exchange and correlation effects. The most widely used schemes are the generalized gradient approximation, GGA, or the local density approximation, LDA. All calculations reported here were performed with the GGA functional of Perdew, Becke and Ernzerhof (PBE) [24], as implemented in the academic version of the CASTEP program [25].

For the calculations ultrasoft pseudopotentials from the CASTEP database were employed. The cut-off for the kinetic energy was 380 eV. The spacing of the Monkhorst–Pack k-point grid was chosen to be smaller than 0.04 $Å^{-1}$, which had been shown to give converged results. We defined that self-consistency had been achieved when the residual stress was <0.02 GPa, the maximal force <0.01 eV/Å and the energy change less than 5×10^{-6} eV/atom. All structural parameters not constrained by the space group symmetry were relaxed simultaneously.

Such full geometry relaxations were performed for the $Bi_2Ga_4O_9$ crystal structure at 14 pressures in the interval between 0 and 25 GPa and at 30, 40, 50 and 100 GPa. Additionally, the crystal structure was optimized at 0 and at 21 GPa after reduction of the symmetry to $P1$, in order to check for a possible phase transition towards an energetically more favorable high-pressure phase.

5. Results

Experimentally determined unit cell parameters of $Bi_2Al_4O_9$, $Bi_2Mn_4O_{10}$ and $Bi_2Ga_4O_9$ as a function of pressure are summarized in Tables 1, 2 and 3, respectively, while those obtained from DFT calculations on $Bi_2Ga_4O_9$ are shown in Table 4. The respective plots of the calculated and experimentally determined pressure dependencies of the normalized unit cell volumes and cell parameters of $Bi_2Ga_4O_9$, $Bi_2Al_4O_9$ and $Bi_2Mn_4O_{10}$ are shown in Fig. 7.

The DFT calculations were performed first during the current study initiating the high-pressure experiments. Hence, we first describe the results of the DFT calculations, followed by the experimental results.

Table 1
Pressure dependencies of the unit cell parameters and volume for $Bi_2Al_4O_9$.

P (GPa)	V (Å^3)	a (Å)	b (Å)	c (Å)
0.0001	356.91(1)	7.7253(1)	8.1128(2)	5.6947(1)
0.0001[a]	356.2	7.7134(1)	8.1139(2)	5.6914(1)
2.74(1)	349.69(1)	7.6625(1)	8.0610(2)	5.6614(1)
3.89(2)	346.53(1)	7.6348(1)	8.0383(2)	5.6466(1)
5.34(2)	342.85(2)	7.6009(2)	8.0107(2)	5.6307(2)
7.10(7)	339.24(1)	7.5667(1)	7.9879(2)	5.6126(1)
8.61(7)	335.83(1)	7.5352(1)	7.9647(1)	5.5958(1)
9.95(5)	333.24(1)	7.5103(2)	7.9475(2)	5.5830(1)
11.71(1)	329.68(1)	7.4763(2)	7.9238(2)	5.5651(1)
13.83(2)	325.81(1)	7.4373(2)	7.9003(2)	5.5450(1)
15.7(1)	322.65(1)	7.4048(2)	7.8803(2)	5.5293(1)
17.63(4)	319.45(1)	7.3700(2)	7.8619(2)	5.5132(1)
19.10(1)	317.29(1)	7.3467(2)	7.8490(2)	5.5024(1)
20.20(1)	316.53(2)	7.3375(3)	7.8447(3)	5.499(2)
22.13(1)	313.22(2)	7.3012(2)	7.8288(3)	5.4797(2)
23.86(9)	310.55(3)	7.2708(4)	7.8128(4)	5.4669(3)
25.19(6)	309.03(2)	7.2517(3)	7.8056(3)	5.4594(2)
27.17(8)	306.44(3)	7.2169(4)	7.7929(5)	5.4487(3)
28.73(6)	303.43(2)	7.1792(4)	7.7816(4)	5.4314(2)

[a] Values at room conditions from Abrahams et al. [8].

Table 2
Pressure dependencies of the unit cell parameters and volume for $Bi_2Mn_4O_{10}$.

P (GPa)	V (Å^3)	a (Å)	b (Å)	c (Å)
0.0001	372.27(1)	7.5608(1)	8.5402(2)	5.7652(1)
0.0001[a]	371.02	7.540(5)	8.534(5)	5.766(5)
2.14(1)	367.24(2)	7.4953(3)	8.5233(3)	5.7485(2) *
3.88(3)	362.23(1)	7.4318(2)	8.5029(2)	5.7316(2)
4.789(2)	360.12(1)	7.4046(2)	8.4940(2)	5.7258(2)
6.32(3)	356.67(1)	7.3581(2)	8.4806(2)	5.7157(1)
7.98(3)	353.69(1)	7.3197(2)	8.4655(2)	5.7079(1)
9.73(7)	349.84(1)	7.2674(2)	8.4502(2)	5.6966(1)
11.34(4)	346.88(3)	7.2266(5)	8.4359(5)	5.6901(3)
12.6(1)	344.77(1)	7.1948(3)	8.4281(2)	5.6857(2)
14.23(8)	342.03(1)	7.1556(3)	8.4133(3)	5.6814(2)
15.33(5)	340.02(3)	7.1204(5)	8.4064(4)	5.6806(3)
16.815(5)	337.62(2)	7.0844(3)	8.3957(3)	5.6763(2)
18.00(4)	336.08(2)	7.0530(3)	8.3915(3)	5.6785(2)
19.05(5)	334.16(2)	7.0245(3)	8.3798(3)	5.6768(3)
20.29(2)	332.13(2)	6.9915(4)	8.3686(4)	5.6765(3)
21.49(4)	330.16(3)	6.9565(5)	8.3653(4)	5.6735(4)
23.14(3)	327.18(7)	6.8783(1)	8.3532(9)	5.6945(6) *
24.594(4)	325.59(6)	6.862(1)	8.3410(9)	5.6887(6)
25.28(6)	325.01(4)	6.850(1)	8.3368(8)	5.6925(6)
25.65(1)	324.06(6)	6.8166(9)	8.3370(8)	5.7024(6) *
26.25(7)	323.96(5)	6.8347(8)	8.3314(7)	5.6893(5)
27.31(3)	321.96(5)	6.8024(8)	8.3200(6)	5.6893(5)
28.57(9)	319.77(4)	6.7730(8)	8.3001(6)	5.6883(5)
29.8(1)	317.91(4)	6.7376(7)	8.2974(7)	5.6866(4)
30.97(8)	315.87(5)	6.7095(8)	8.2875(8)	5.6805(4)
31.97(6)	314.19(6)	6.678(1)	8.280(1)	5.6818(6)
33.00(9)	313.40(7)	6.645(1)	8.286(1)	5.6913(8)
34.38(9)	311.84(5)	6.604(1)	8.278(1)	5.7037(8)

Values from decompression measurements are marked with asterisks.
[a] Values at room conditions from Niizeki and Wachi [11].

5.1. DFT calculations

The predicted unit cell parameters of $Bi_2Ga_4O_9$ at ambient conditions are slightly overestimated (up to 2% for the cell parameters and about 5% for the unit-cell volume) compared to the experimental results (Tables 3 and 4). This is typical for DFT-GGA calculations such as those performed here. The pressure evolution of the calculated cell parameters of $Bi_2Ga_4O_9$ (Table 4,

Table 3
Pressure dependencies of the unit cell parameters and volume for $Bi_2Ga_4O_9$.

P (GPa)	V (Å^3)	$V/2$ (Å^3)[a]	a (Å)	b (Å)	c (Å)	$c/2$ (Å)[a]
0.0001	388.625(8)		7.9360(1)	8.3021(1)	5.8985(1)	
0.0001[b]	388.77		7.934	8.301	5.903	
0[c]	409.4		8.011	8.474	6.030	
2.40(1)	379.91(1)		7.8537(2)	8.2438(2)	5.8678(1) *	
4.27(1)	374.13(2)		7.7951(3)	8.2069(2)	5.8483(2) *	
5.34(1)	364.44(2)		7.7158(3)	8.1387(3)	5.8034(2) *	
6.6(1)	367.62(1)		7.7253(2)	8.1680(2)	5.8260(2) *	
7.61(4)	363.686(8)		7.6866(2)	8.1412(1)	5.8117(1)	
7.64(1)	363.88(1)		7.6882(2)	8.1427(1)	5.8125(1)	
8.25(5)	362.17(1)		7.6688(2)	8.1336(2)	5.8064(1)	
9.30(1)	359.07(1)		7.6313(1)	8.1178(1)	5.7962(1)	
10.69(9)	355.80(1)		7.5919(2)	8.1006(2)	5.7855(1)	
11.50(2)	353.917(8)		7.5676(1)	8.0926(2)	5.7790(1)	
12.3(2)	351.18(1)		7.5325(1)	8.0802(2)	5.7699(1)	
12.41(8)	352.20(2)		7.5365(3)	8.0906(3)	5.7761(2) *	
13.8(4)	349.10(2)		7.4917(1)	8.0797(1)	5.7673(1) *	
15.18(6)	345.05(2)		7.4440(3)	8.0567(3)	5.7532(2)	
15.73(2)	343.89(2)		7.4250(2)	8.0549(2)	5.7500(2)	
16.07(4)		340.94(7)	7.2436(6)	8.1378(4)		5.7838(9) *
16.88(3)		337.65(4)	7.1862(4)	8.1403(3)		5.7720(5)
18.01(3)		335.22(3)	7.1313(3)	8.1461(2)		5.7705(4)
18.74(3)		333.47(4)	7.0982(3)	8.1469(3)		5.7666(5)
19.32(2)		332.26(4)	7.0729(3)	8.1469(3)		5.7662(4)
19.91(4)		330.78(5)	7.0398(3)	8.1494(3)		5.7658(5)
20.35(2)		329.76(5)	7.0199(3)	8.1492(3)		5.7644(5)
20.49(4)		329.67(5)	7.0119(3)	8.1582(3)		5.7630(5) *
20.91(3)		328.46(4)	6.9945(3)	8.1491(3)		5.7625(5)
21.13(2)		328.05(5)	6.9882(3)	8.1482(3)		5.7612(5)
21.78(8)		326.96(5)	6.9701(4)	8.1485(3)		5.7568(6)
22.70(6)		325.42(5)	6.9506(4)	8.1457(3)		5.7476(6)
23.98(2)		322.72(5)	6.9061(3)	8.1446(4)		5.7375(7)
25.37(3)		320.42(6)	6.8642(4)	8.1405(5)		5.7342(7)
27.01(3)		317.87(6)	6.8243(4)	8.1325(6)		5.7276(4)
28.68(3)		315.41(8)	6.7871(4)	8.1245(4)		5.7199(6)
30.30(3)		312.82(5)	6.7506(3)	8.1195(3)		5.7072(6)
32.55(9)		310.07(6)	6.7097(4)	8.1097(4)		5.6983(7)
34.89(7)		306.28(6)	6.6581(5)	8.0966(4)		5.6815(7)

Values from decompression measurements are marked with asterisks. The c-axis and unit cell volume are doubled at the phase transition. Here, normalized values are given for better comparison with the low-pressure phase.
[a] High pressure phase.
[b] Values at room conditions from Mueller-Buschbaum and de Beaulieu [21].
[c] DFT, this study.

Table 4
Pressure dependencies of the unit cell parameters and volume for $Bi_2Ga_4O_9$ from DFT calculations.

P (GPa)	V (Å^3)	a (Å)	b (Å)	c (Å)
0	409.4	8.011	8.474	6.030
2	400.8	7.928	8.432	5.996
5	387.7	7.787	8.360	5.955
10	369.8	7.550	8.297	5.904
12	364.0	7.473	8.274	5.888
14	357.7	7.353	8.271	5.881
15	355.0	7.307	8.266	5.877
17	348.5	7.148	8.279	5.884
18	345.4	7.068	8.285	5.898
20	339.0	6.883	8.300	5.934
21	336.8	6.838	8.298	5.936
21	337.0	6.843	8.297	5.935
22	334.4	6.777	8.301	5.944
25	328.0	6.628	8.318	5.952
30	319.8	6.496	8.308	5.926
40	307.3	6.340	8.278	5.855
50	296.6	6.217	8.255	5.779
100	261.0	5.857	8.162	5.459

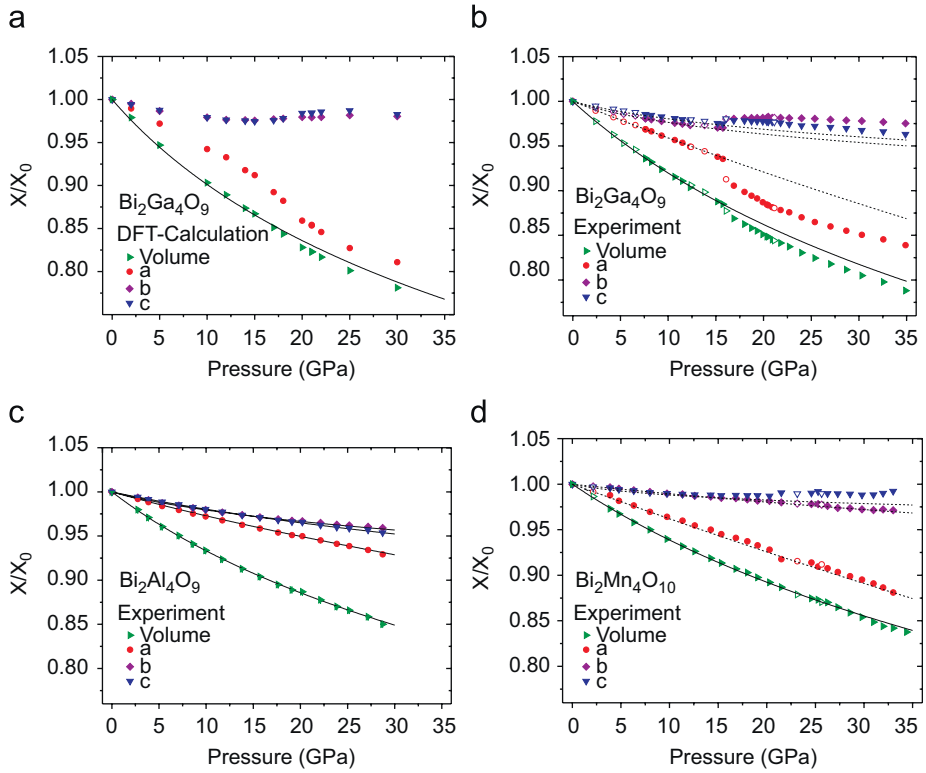

Fig. 7. (Color online) Pressure dependencies of the normalized unit cell volumes and lattice parameters for (a) $Bi_2Ga_4O_9$ obtained from quantum mechanical calculations using density functional theory, (b) $Bi_2Ga_4O_9$ from experiments, (c) $Bi_2Al_4O_9$, and (d) $Bi_2Mn_4O_{10}$. (a) The plot range of the DFT data is limited to 35 GPa for a better comparison with the experimental data. (b) For the high-pressure phase of $Bi_2Ga_4O_9$ ($p>16$ GPa) the values of $c/(2c_0)$ and $V/(2V_0)$ are plotted for a better illustration. The solid lines show fits with a 3rd-order Birch–Murnaghan equation of state, dashed lines represent fits to the Vinet equation of state. For $Bi_2Ga_4O_9$ only the fits to the low-pressure data up to 15 GPa are plotted. Open symbols show the values at released pressure. Error bars are smaller than the symbol size.

Fig. 7) shows the same trends as the experimental data up to about 15 GPa, with the *a* axis being the most compressible and the *b* and *c* axes showing about the same compressibility. In the pressure range between 15 and 25 GPa, an unusual change in the structural compression is observed, with the *a* axis becoming even more compressible and the *b* and *c* axes expanding as pressure increases (Fig. 7). Above 25 GPa the cell parameters compress continuously again (Table 4). The unit cell volume does not show an observable discontinuity on compression within the precision of our calculations. Geometry optimizations of the low-pressure crystal structure in space group *Pbam* were stable up to a pressure of 100 GPa. Relaxations in space group *P*1 (at 0 and 21 GPa) did not give any indication of a symmetry change or a high-pressure phase transition. This procedure is generally indicative of the absence of a displacive Γ-point structural phase transition. Due to the imposition of periodic boundary conditions, structural phase transitions involving an enlargement of the unit cell (such as zone boundary transitions) cannot be discovered. Such transitions require alternative, computationally much more expensive approaches such as mode-following for soft mode transitions or searches of the energy landscape. However, already in an earlier study, such an unusual behavior had later led to the experimental detection of a structural phase transition [26]. Hence, the prediction of the unusual compression between 15 and 25 GPa in $Bi_2Ga_4O_9$ was the driving force for the subsequent experiments on this and the related compounds by powder and single-crystal X-ray diffraction in the pressure range up to 35 GPa.

5.2. Phase transition

For $Bi_2Ga_4O_9$ a phase transition was observed experimentally at about 16 GPa, which causes significant changes of the diffraction pattern and the appearance of additional reflections (Fig. 8). At the phase transition the symmetry is reduced from space group *Pbam* to the maximal non-isomorphic subgroup of class IIb *Pbnm* (with $c' = 2c$), and hence it is associated with a doubling of the *c* axis and of the unit-cell volume ($a = 7.1862(4)$ Å, $b = 8.1403(3)$ Å, $c = 11.5440(5)$ Å, $V = 675.3(4)$ Å^3 at 16.88(3) GPa, Table 3). This explains the failure of the DFT-model to predict the correct high-pressure phase, as the imposition of periodic boundary conditions prevents the doubling of a cell-parameter during the geometry optimization. The crystal structure of the high-pressure phase of $Bi_2Ga_4O_9$ was solved from single-crystal high-pressure data and will be described in a future publication. The phase transition is fully reversible and no hysteresis was observed upon decompression within the precision of our data (Table 3, Fig. 7). At the phase transition the *a* cell parameter is strongly reduced, while the *b* and *c* parameters are slightly increased, resulting in an overall slight decrease of the unit cell volume. This behavior is similar to the unusual changes of structural compression obtained from the DFT model. In contrast to the behavior of $Bi_2Ga_4O_9$, no phase transition was observed in either $Bi_2Al_4O_9$ or $Bi_2Mn_4O_{10}$ up to 29 and 35 GPa, respectively.

5.3. Bulk compressibility

The parameters obtained from the EOS fits, as well as earlier experimental and theoretical values for $Bi_2Ga_4O_9$ [2], are summarized in Table 5. The $f-F$ plots for $Bi_2Al_4O_9$, $Bi_2Mn_4O_{10}$ and $Bi_2Ga_4O_9$ are shown in Fig. 9. The positive slope in the $f-F$ evolution of $Bi_2Al_4O_9$ indicates that the pressure derivative of the bulk modulus, K', is larger than 4. This implies that the use of a 3rd order BM-EOS is appropriate. The $f-F$ plots for $Bi_2Mn_4O_{10}$ and the low- and high-pressure phases of $Bi_2Ga_4O_9$ show a nearly

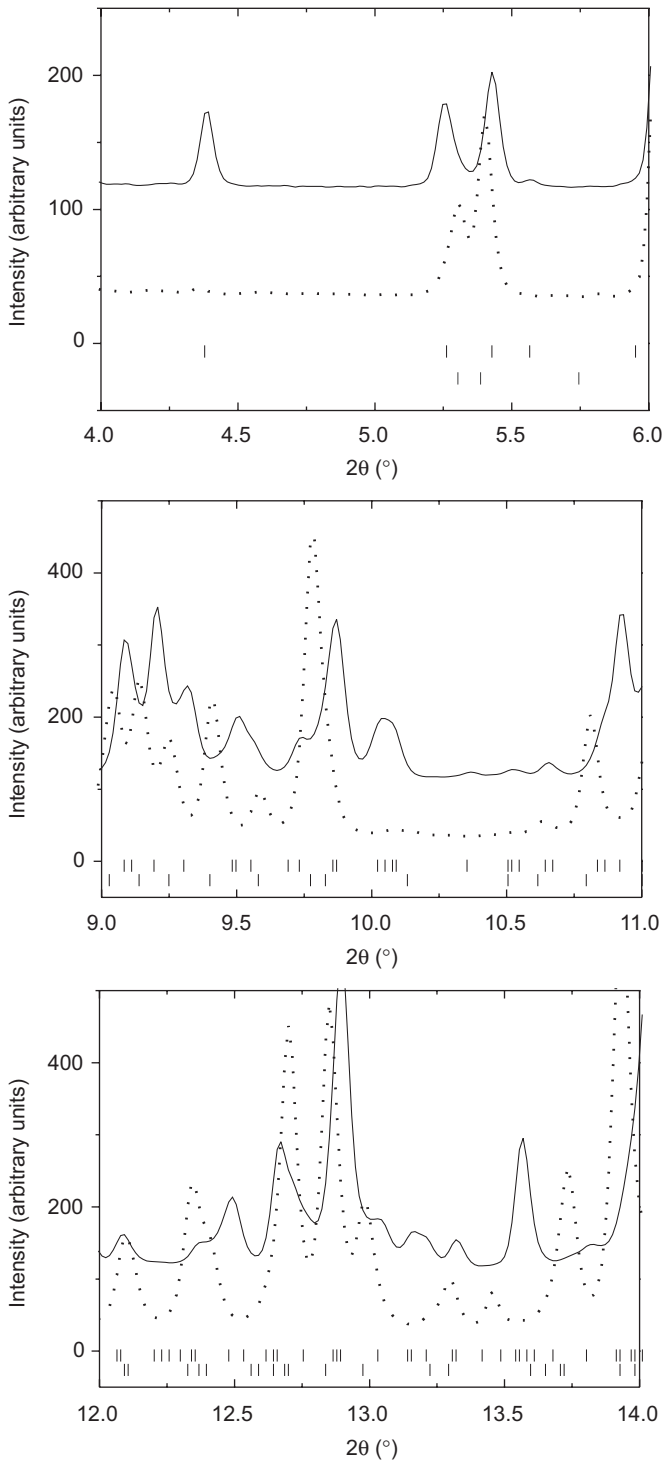

Fig. 8. X-ray powder diffraction patterns for $Bi_2Ga_4O_9$ at 15.73(2) GPa (dotted lines) and 16.88(3) GPa (solid lines) showing the occurrence of new peaks and significant changes of the diffraction pattern during the phase transition. Vertical bars show the positions of the allowed Bragg reflections of the high-pressure phase (top row) and low-pressure polymorph (bottom row).

horizontal behavior which indicates a K' close to 4. The compressibilities of the low- and high-pressure phases of $Bi_2Ga_4O_9$ are very similar and result in only small differences between the BM-EOS fits (Fig. 9) and in the values for the bulk moduli of $K_0 = 102(8)$ and 102(7) GPa, for the low- and the high-pressure phase, respectively. The low-pressure value of $K_0 =$ 102(8) GPa obtained here, is in good agreement with the value of $K_0 = 101.9$ GPa obtained experimentally from a single crystal using resonant ultrasound spectroscopy (RUS) [2]. The bulk modulus obtained from a BM-EOS fit to the pressure-dependent DFT data of this study is significantly lower with 85(2) GPa than obtained by experiment (this study, [2]) or from the calculation of the elastic constants using the same model parameters and the stress–strain method ([2], Table 5).

Table 5
Volume, V_0, bulk modulus, K_0, and the first derivative of the bulk modulus, K', for $Bi_2Al_4O_9$, $Bi_2Mn_4O_{10}$ and $Bi_2Ga_4O_9$ obtained from a fit with a 3rd-order Birch–Murnaghan equation of state.

Compound	V_0 (Å^3)	K_0 (GPa)	K'	p_{max} (GPa)
$Bi_2Al_4O_9$	356.93(9)	122(2)	4.9(3)	28.73(6)
$Bi_2Mn_4O_{10}$	372.27(1)	138(1)	4.2(2)	34.38(9)
$Bi_2Ga_4O_9$ low-p phase	388.63(3)	102(8)	3.8(2)	16.07(4)
$Bi_2Ga_4O_9$ X-ray and RUS[a]	388.78	101.9	–	–
$Bi_2Ga_4O_9$ DFT[b]	409.35	109	–	–
$Bi_2Ga_4O_9$ DFT[c]	409.4(1)	85(2)	3.0(3)	15
$Bi_2Ga_4O_9$ high-p phase	768(2)	102(7)	3.6(3)	34.89(7)

[a] X-ray and RUS-experiment from Schreuer et al. [2].
[b] DFT-GGA calculation of the elastic constants from Schreuer et al. [2].
[c] Pressure-dependent DFT-GGA calculations from this study.

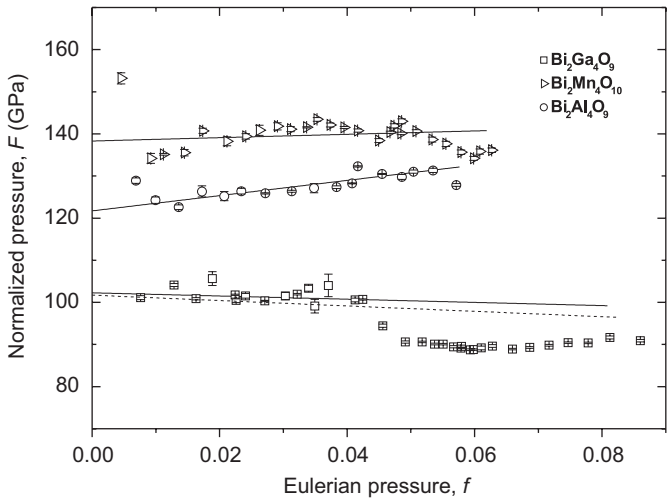

Fig. 9. Pressure-volume data as a plot of the dependence of Eulerian strain f on the normalized pressure F of $Bi_2Al_4O_9$ (circles), $Bi_2Mn_4O_{10}$ (triangles) and $Bi_2Ga_4O_9$ (squares). The unit-cell volume of the high-pressure phase of $Bi_2Ga_4O_9$ was divided by two for a better visualization. Third-order BM-EOS fits to data are represented by solid lines. The fit to the high-pressure phase of $Bi_2Ga_4O_9$, also using a 3rd-order BM-EOS, is represented by the dashed line. The offset of the fit of the high-pressure phase from the experimental data is due to the use of different values for V_0 in the calculation of the $f-F$ values. The experimental data were calculated using the unit cell volume of the low-pressure phase at ambient conditions for V_0, while the extrapolated unit-cell volume of the high-pressure phase to ambient conditions was used in the fit.

5.4. Linear compressibility

For all the compounds, the lattice parameter a is the most compressible (Fig. 7). At pressures up to 16 GPa, the compressibilities of the b and c parameters behave similarly for $Bi_2Al_4O_9$ and $Bi_2Mn_4O_{10}$. In the case of $Bi_2Ga_4O_9$, the b axis is more compressible than the c axis in the low-pressure phase. Above the

phase transition, the c lattice parameter of the high-pressure phase is slightly more compressible than the b parameter.

Slight differences in the compressibilities of the b and c axes of $Bi_2Al_4O_9$ and $Bi_2Mn_4O_{10}$, which are not obvious in the $p-V$ plots (Fig. 7), are apparent in the $f-F$ plots. The $f-F$ plots calculated from the pressure dependencies of the cell parameters of $Bi_2Al_4O_9$, $Bi_2Mn_4O_{10}$ and the low-pressure phase of $Bi_2Ga_4O_9$ are shown in Fig. 10. The values for the linear modulus of the cell axes can be obtained from the intercepts of the linear regressions on the F axis and are summarized in Table 6. An estimate is given for the corresponding values of K' from the slopes of the lines. It is obvious that the slopes of the linear $f-F$ data of the b and c cell parameters are strongly positive in all compounds. However, the $f-F$ data of the a axis show a negative ($Bi_2Mn_4O_{10}$ and $Bi_2Ga_4O_9$) or slightly positive slope ($Bi_2Al_4O_9$).

The strongest anisotropy in the linear compressibilities is observed for $Bi_2Mn_4O_{10}$, where nearly all compression seems to occur along the a axis (Table 6). At ambient conditions the unit cell of $Bi_2Mn_4O_{10}$ is more strongly distorted with respect to $Bi_2Al_4O_9$ and $Bi_2Ga_4O_9$, with the b axis being the largest of all the three compounds and the a axis the smallest. This is due to tilting of the MnO_5 pyramids as compared to the GaO_4 tetrahedra. Nevertheless, this distortion does not reduce the strong compressibility along the a axis.

6. Discussion

6.1. Bulk compressibility

A comparison of the bulk modulus and unit cell volumes of isotypic $Bi_2Al_4O_9$ ($V_0 = 356.93(9)\,Å^3$, $K_0 = 122(2)\,GPa$) and $Bi_2Ga_4O_9$ ($V_0 = 388.63(3)\,Å^3$, $K_0 = 102(8)\,GPa$) agrees with the expected tendency that the higher compressibility is observed for the compound with the larger unit-cell volume [27], namely $Bi_2Ga_4O_9$ (Table 5). The difference in unit-cell volumes can be explained by the Al/Ga substitution, taking into account the different ionic radii of Al^{3+} and Ga^{3+}. In $Bi_2M_4O_9$ ($M = Al, Ga$) the M ions are in equal amounts in fourfold coordination (M_{IV}) and sixfold coordination (M_{VI}). The ionic radii of Al^{3+} in fourfold and sixfold coordination are $Al_{IV} = 0.39\,Å$ and $Al_{VI} = 0.535\,Å$, respectively, while for Ga^{3+} they are $Ga_{IV} = 0.47\,Å$ and $Ga_{VI} = 0.62\,Å$ [28].

$Bi_2Mn_4O_{10}$ ($V_0 = 372.27(1)\,Å^3$, $K_0 = 138(1)\,GPa$, Table 5) cannot be compared directly to $Bi_2Al_4O_9$ and $Bi_2Ga_4O_9$, as it has a slightly different stoichiometry. In a unit cell of $Bi_2Mn_4O_{10}$ there is the same quantity of Mn^{3+} ions in fivefold coordination as Mn^{4+} ions in sixfold coordination [12]. The cation radii ($Mn^{3+}_V = 0.58\,Å$, $Mn^{4+}_{VI} = 0.53\,Å$ [28]) indicate that the volumes of the metal polyhedra will be similar to $Bi_2Al_4O_9$ and $Bi_2Ga_4O_9$, and in fact the unit cell volume of $Bi_2Mn_4O_{10}$ is in between those of $Bi_2Al_4O_9$ and $Bi_2Ga_4O_9$. Due to the 'additional' oxygen, the space filling of $Bi_2Mn_4O_{10}$ is higher than that of the two other compounds, and hence the larger bulk modulus with respect to $Bi_2Al_4O_9$ and $Bi_2Ga_4O_9$ is explained (Table 5).

A comparison with the aluminum oxides and aluminum silicates from the family of sillimanite- and mullite-type crystal structures shows that the compounds investigated here are much more compressible than sillimanite and mullite *sensu stricto*, where experimental values for K_0 range from 164 to 176 GPa for sillimanite [29–33,10] and from 166.5 to 174 GPa for different mullites [34–38]. This discrepancy can be attributed to the existence of the large Bi^{3+} cations and the very compressible stereochemically active $Bi6s^2$ lone electron pairs, and to a number of structural voids [2]. The same phenomenon is present in other systems such as BiB_3O_6 [39].

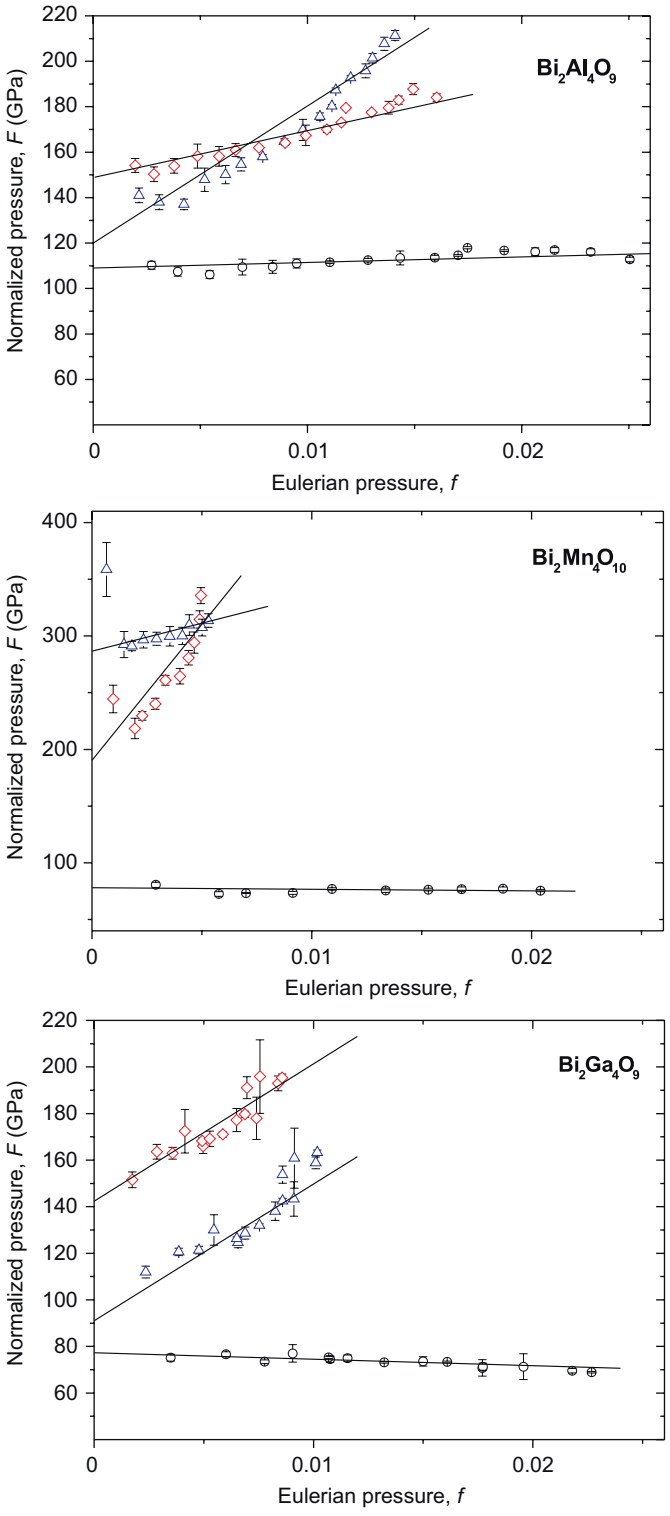

Fig. 10. The pressure dependencies of the cell parameters [a (circles), b (triangles), and c (diamonds)] of $Bi_2Al_4O_9$ (top), $Bi_2Mn_4O_{10}$ (middle) and $Bi_2Ga_4O_9$ (bottom) are plotted as a normalized pressure F against the Eulerian strain f. For $Bi_2Mn_4O_{10}$ the maximal pressure is limited to 16 GPa in this plot. In this pressure range the pressure-transmitting medium, neon, behaves quasi-hydrostatic. For $Bi_2Ga_4O_9$ only data of the low-pressure phase are included in the plot. Lines are plotted as guides to the eye.

6.2. Linear compressibility

The b and c axes are quite incompressible due to the orientation of the chains of edge-sharing MO_6- and ZO_6-octahedra, in $Bi_2M_4O_9$

Table 6
Bulk modulus of the unit cell parameters for $Bi_2Al_4O_9$, $Bi_2Mn_4O_{10}$ and $Bi_2Ga_4O_9$ obtained from an intercept of the linear regressions to the experimental $f-F$ data at $f=0$.

Compound	K_{a0} (GPa)	K'_{a0}
$Bi_2Al_4O_9$	108	≈ 4
$Bi_2Mn_4O_{10}$	79	<4
$Bi_2Ga_4O_9$	78	<4
	K_{b0} (GPa)	K'_{b0}
$Bi_2Al_4O_9$	120	>4
$Bi_2Mn_4O_{10}$	281	>4
$Bi_2Ga_4O_9$	91	>4
	K_{c0} (GPa)	K'_{c0}
$Bi_2Al_4O_9$	148	>4
$Bi_2Mn_4O_{10}$	179	>4
$Bi_2Ga_4O_9$	141	>4

and $Bi_2Z_2M_2O_{10}$ respectively, running parallel to the c axis, and due to a strong interconnection via corrugated chains of type $\cdots-Bi-O-Bi-O-\cdots$ parallel to the b axis (Fig. 2). In contrast to the strong Bi–O bonding scheme parallel to the b axis, strong Bi–O bonds are alternating with very weak Bi–O bonds parallel to the a axis. These are indicated by dotted lines in Fig. 2. The direction of largest compression is along the a axis. The long and presumably weak Bi–O bonds are oriented along this direction, and hence it seems reasonable to conclude that the greatest changes of these structure types on compression occur in the strongly distorted Bi^{3+} coordination. This agrees with the expected large flexibility and compressibility of the lone electron pairs, which are alternating in channels with the oxygen atoms joining two tetrahedra in the $Bi_2M_4O_9$ structure or two pyramids in $Bi_2Mn_4O_{10}$ (Fig. 2).

A comparison of the linear compressibilities of $Bi_2Ga_4O_9$ obtained in this study with the elastic constants measured by RUS [2] is coherent with respect to the behavior of the a and c cell parameters. The c_{11} elastic constant is the softest, which agrees with the strongest compressibility observed along the a axis, and c_{33} is the stiffest, which again agrees with the high incompressibility of the octahedral chains oriented parallel to the c axis. The behavior of the b axis is not so obvious from our data. While the b axis seems to be nearly as incompressible as the c axis in Fig. 7, the extrapolation of a fit to the linear $f-F$ data indicates a pronounced softness of the b axis with respect to the c axis (Fig. 10). This would agree with the anisotropy of the elastic constants measured with RUS, in which the value of c_{22} was much closer to c_{11} than to c_{33}.

An extension of the comparative analysis to the structurally related phases sillimanite and mullites shows, that in all of these compounds the stiffest direction is along the c axis, which is the direction of the octahedral chains (e.g. [30,35–38,10]). In sillimanite and mullites, the b axis was found to be the most compressible direction. This was attributed to anisotropic compression of the AlO_6 octahedra and a rotation of the octahedral chains, which form an angle of about 30° with the b axis (e.g., [10,30,36]). In contrast, by far the largest compression is observed along the a axis in $Bi_2M_4O_9$, $M=Al, Ga$, and $Bi_2Mn_4O_{10}$. This points towards a main contribution of the asymmetric environment of Bi^{3+} on the structural compression mechanism.

6.3. Phase transition

Symmetry relations between the low- and the high-pressure phase of $Bi_2Ga_4O_9$ show that the phase transition is non-ferroic [40]. Hence the strains will be second-order in the order parameter. During the zone-boundary phase transition ($c'=2c$) the orthorhombic point group symmetry is retained and the strain is non-symmetry breaking.

The pressure dependencies of the volume strain V_s, with $V_s=(V-V_0)/V_0$, and of the strain components e_{11}, e_{22} and e_{33}, with $e_{ii}=a_i/a_{i,0}-1$, as well as the pressure dependencies of their square roots, are plotted in Figs. 11 and 12, respectively. V and a_i are the unit cell volume and unit cell parameters of the low-symmetry phase at given pressures, and V_0 and $a_{i,0}$ of the high-symmetry phase extrapolated to the same pressure from the EOS fits. An extrapolation to very high pressures is associated with an increased uncertainty, and seems to be inappropriate for our data as an increased curvature of the EOS would be expected at higher pressures corresponding to a higher value of K'. However, it seems to be appropriate for the pressure range between 15 and 20 GPa, which we will use for our discussion only. It appears that the squared volume strain varies linearly with pressure (Fig. 11), such that the volume strain varies as $(P-P_c)^{1/2}$, where P_c is the pressure at which the phase transition occurs. Since the volume strain is proportional to Q^2, with Q being the order parameter, it appears to be a tricritical phase transition with $Q\propto(P-P_c)^{1/4}$. In contrast, the behavior of the strain components points towards a

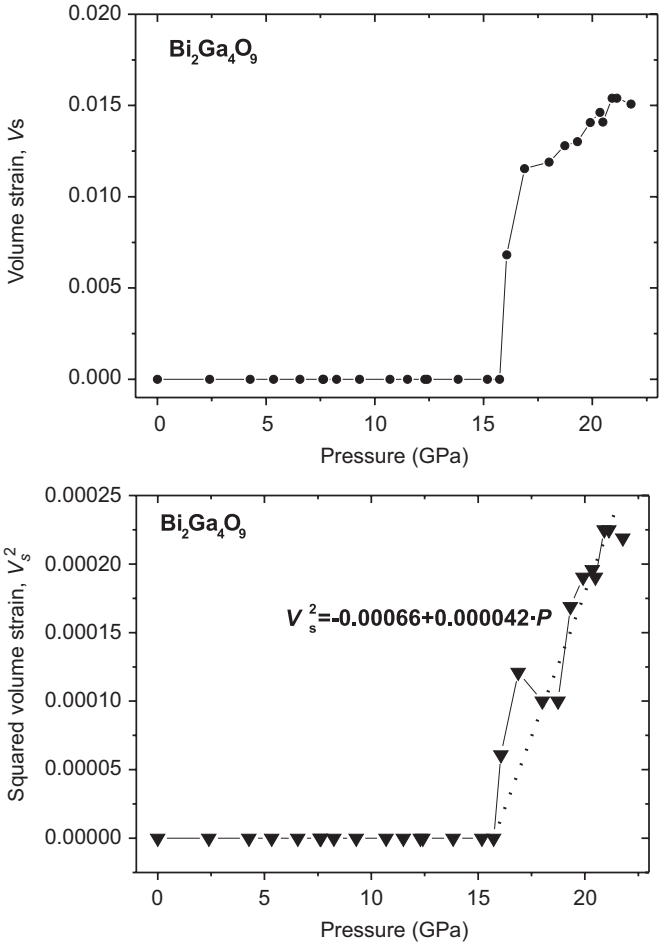

Fig. 11. Pressure dependencies of the (top) volume strain and (bottom) squared volume strain of $Bi_2Ga_4O_9$. The dotted line represents a linear fit through the transition pressure. The linear equation is given in the plot.

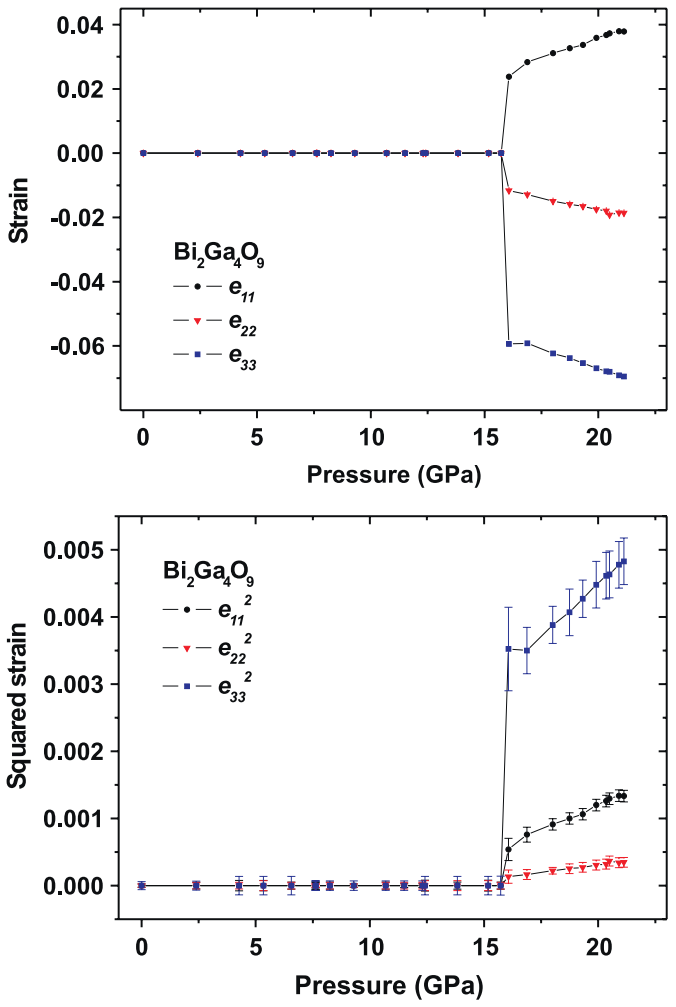

Fig. 12. (Color online) Pressure dependencies of (top) the strain components e_{11} (black circles), e_{22} (red triangles) and e_{33} (blue squares) of $Bi_2Ga_4O_9$ and (bottom) their square roots e_{11}^2, e_{22}^2 and e_{33}^2. Top: error bars are smaller than the symbol size.

phase transition which is weakly first order (Fig. 12). In comparison with the huge number of temperature-induced phase transitions only few examples of the application of Landau theory on high-pressure phase transitions exist up to now. The pressure evolution of the lattice parameters is generally measured in much coarser intervals with respect to the temperature steps possible, which can be applied with temperature-induced phase transitions. Hence, much smaller steps in pressure would be required to definitely distinguish the character of the phase transition to be tricritical or first-order.

The occurrence of a phase transition in $Bi_2Ga_4O_9$ at about 16 GPa opens up the question, of why no phase transition is observed in the other two compounds, $Bi_2Al_4O_9$ and $Bi_2Mn_4O_{10}$, at pressures up to even 29 and 35 GPa, respectively. Obviously, a pressure-induced change of the asymmetric $6s^2$ lone electron pair of Bi^{3+} towards a symmetric environment, as it was discussed for $CsGeCl_3$ [15], is not the reason for the phase transition of $Bi_2Ga_4O_9$. The higher stability of $Bi_2Mn_4O_{10}$ at high pressure can be explained by the additional oxygen atom and hence the higher coordination of the Mn-polyhedra in this structure, Mn^{3+} showing fivefold coordination. As a consequence, two $Mn^{3+}O_5$ pyramids share a common edge which is oriented parallel to the *c* axis. This makes the structure stiffer (see bulk modulus in Table 5) and more resistant to phase changes. Instead, the $M^{3+}O_4$ tetrahedra in the $Bi_2M_4O_9$ structure are connected via a bridging oxygen atom, forming an unfavorable straight *M*–O–*M* angle of 180° (Fig. 3), which is more flexible and tends towards destabilization at high pressure.

In contrast, $Bi_2Al_4O_9$ is isotypic to $Bi_2Ga_4O_9$ showing the same unfavorable straight Al–O–Al angle between the Al_2O_7 groups of tetrahedra. As the unit-cell volume of $Bi_2Al_4O_9$ is smaller than that of $Bi_2Ga_4O_9$ and the bulk modulus is larger, a similar phase transition would be expected at a higher pressure than 16 GPa according to the pressure-homologue rule [41,42]. In $Bi_2Ga_4O_9$ a volume reduction of $\approx 12.3\%$ was achieved in advance of the phase transition. Considering the same reduction of the unit cell volume for $Bi_2Al_4O_9$, a similar phase transition is assumed to occur at ≈ 23 GPa. As no phase transition is observed up to at least 29 GPa, $Bi_2Al_4O_9$ is much more stable at increased pressure than isotypic $Bi_2Ga_4O_9$. This might be due to the smaller size of the Al^{3+} cations in the tetrahedral coordination by four oxygen atoms compared with the size of the Ga^{3+} cations. If this approach is correct a similar phase transition should also occur in $Bi_2Fe_4O_9$, since Fe^{3+} has a slightly larger ionic radius (0.49 Å) than Ga^{3+} (0.47 Å, ionic radii are for tetrahedral coordination of the cations) [28]. This assumption is intended to be checked by studying the high-pressure behavior of $Bi_2Fe_4O_9$.

7. Conclusions

We have studied the high-pressure behavior of the compounds $Bi_2Al_4O_9$, $Bi_2Mn_4O_{10}$ and $Bi_2Ga_4O_9$ by *in situ* powder synchrotron X-ray diffraction using the diamond anvil cell technique to generate pressures up to 29 GPa for $Bi_2Al_4O_9$, and up to 35 GPa for $Bi_2Mn_4O_{10}$ and $Bi_2Ga_4O_9$. $Bi_2Al_4O_9$ and $Bi_2Mn_4O_{10}$ are structurally stable to the highest pressure obtained. However, a phase transition is observed in $Bi_2Ga_4O_9$ at approximately 16 GPa. This effect can be attributed to the larger size of the Ga^{3+} cation tending towards a higher coordination than four at pressure increase. The structure of the high-pressure phase of $Bi_2Ga_4O_9$ was solved from single-crystal structure analysis in our group and a detailed description of the structural compression before and at the phase transition, derived from quantum mechanical DFT-calculations and experiment, will be given in a subsequent manuscript.

Acknowledgments

The authors acknowledge financial support from the DFG (WI1232/25-1 and WI1232/26-1 within the project SPP1236, and MU1006/8-1), and from the DAAD. Also, we are grateful to the ESRF for beamtime and financial support. AF thanks the Christiane Nüsslein-Volhard foundation for financial support. We would like to thank Martin Dove (University of Cambridge) for helpful discussions.

References

[1] R.X. Fischer, H. Schneider, The mullite-type family of crystal structures, in: H. Schneider, S. Komarneni (Eds.), Mullite, Wiley-VCH, Weinheim, 2005, pp. 1–140.
[2] J. Schreuer, M. Burianek, M. Mühlberg, B. Winkler, D.J. Wilson, H. Schneider, Crystal growth and elastic properties of orthorhombic $Bi_2Ga_4O_9$, J. Phys. Condens. Matter 18 (2006) 10977–10988.
[3] G. Blasse, O.B. Ho, On the luminescence of bismuth aluminate ($Bi_2Al_4O_9$), J. Lumin. 21 (1980) 165–168.
[4] V.V. Volkov, A.V. Egorysheva, Y.F. Kargin, V.I. Solomonov, S.G. Mikhailov, S.I. Buzmakova, B.V. Shul'gin, V.M. Skorikov, Synthesis and luminescent properties of $Bi_2Ga_4O_9$ single crystals, Inorg. Mater. 32 (1996) 455–458.
[5] V.V. Volkov, A.V. Egorysheva, Photoluminescence in fast-response $Bi_2Al_4O_9$ and $Bi_2Ga_4O_9$ oxide scintillators, Opt. Mater. 5 (1996) 273–277.

[6] I. Bloom, M.C. Hash, J.P. Zebrowski, K.M. Myles, M. Krumpelt, Oxide-ion conductivity of bismuth aluminates, Solid State Ionics 53–56 (1992) 739–747.
[7] S. Zha, J. Cheng, Y. Liu, X. Liu, G. Meng, Electrical properties of pure and Sr-doped $Bi_2Al_4O_9$ ceramics, Solid State Ionics 156 (2003) 197–200.
[8] I. Abrahams, A.J. Bush, G.E. Hawkes, T. Nunes, Structure and oxide ion conductivity mechanism in $Bi_2Al_4O_9$ by combined X-ray and high-resolution neutron powder diffraction and ^{27}Al solid NMR, J. Solid State Chem. 147 (1999) 631–636.
[9] D.M. Kerrick, The Al_2SiO_5 polymorphs, in: P.H. Ribbe (Ed.), Reviews in Mineralogy, vol. 22, Mineralogical Society of America, 1990, pp. 1–406.
[10] J.B. Burt, N.L. Ross, R.J. Angel, M. Koch, Equations of state and structures of andalusite to 9.8 GPa and sillimanite to 8.5 GPa, Am. Mineral. 91 (2006) 319–326.
[11] N. Niizeki, M. Wachi, The crystal structure of $Bi_2Mn_4O_9$, $Bi_2Al_4O_9$ and $Bi_2Fe_4O_9$, Z. Kristallogr. 127 (1968) 173–187.
[12] N. Nguyen, M. Legrain, A. Ducouret, B. Raveau, Distribution of Mn^{3+} and Mn^{4+} species between octahedral and square pyramidal sites in $Bi_2Mn_4O_{10}$-type structure, J. Mater. Chem. 9 (1999) 731–734.
[13] P. Eckerlin, J. Liebertz, Darstellung und kristallographische Daten von $Bi_2Al_4O_9$-Einkristallen, Naturwissenschaften 52 (1965) 450.
[14] S.K. Filatov, S.V. Krivovichev, Y.V. Aleksandrova, R.S. Bubnova, A.V. Egorysheva, P. Burns, Y.F. Kargin, V.V. Volkov, Crystal-structure refinement, thermal expansion, and chemical distortion of $Bi_2Ga_4O_9$, Russ. J. Inorg. Chem. 51 (2006) 878–883.
[15] B. Winkler, V. Milman, M.-H. Lee, Pressure-induced change of the stereochemical activity of a lone electron pair, J. Chem. Phys. 108 (1998) 5506–5509.
[16] R. Le Toullec, J.P. Pinceaux, P. Loubeyre, The membrane diamond anvil cell: a new device for generating continuous pressure and temperature variations, High Pressure Res. 1 (1988) 77–90.
[17] H. Mao, P. Bell, J. Shaner, D. Steinberg, Specific volume measurement of Cu, Mo, Pd, and Ag and calibration of the ruby R_1 fluorescence pressure gauge from 0.06 to 1 Mbar, J. Appl. Phys. 49 (1978) 3276–3283.
[18] A.P. Hammersley, S.O. Svensson, M. Hanfland, A.N. Fitch, D. Hausermann, Two-dimensional detector software: from real detector to idealised image or two-theta scan, High Pressure Res. 14 (1996) 235–248.
[19] K. Syassen, DATLAB, Version 1.37d MPI/FKF Stuttgart, Germany, 2005.
[20] A.C. Larson, R.B. Von Dreele, GSAS, Report LAUR, Los Alamos National Laboratory, 1994, pp. 86–748.
[21] H. Mueller-Buschbaum, D.C. de Beaulieu, Zur Besetzung von Oktaeder- und Tetraederpositionen in $Bi_2Ga_2Fe_2O_9$, Z. Naturforsch. B Chem. Sci. 33 (1978) 669–670.
[22] R.J. Angel, EOS-FIT, Version 4.2, 1998.
[23] R.J. Angel, Equations of state, in: R.M. Hazen, R.T. Downs (Eds.), High-Temperature and High-Pressure Crystal Chemistry, Reviews in Mineralogy and Geochemistry, vol. 41, Mineralogical Society of America, 2000, pp. 35–59.
[24] J.P. Perdew, K. Burke, M. Ernzerhof, Generalized gradient approximation made simple, Phys. Rev. Lett. 77 (1996) 3865–3868.
[25] S.J. Clark, M.D. Segall, C.J. Pickard, P.J. Hasnip, M.J. Probert, K. Refson, M.C. Payne, First principles methods using CASTEP, Z. Kristallogr. 220 (2005) 567–570.
[26] A. Friedrich, K. Knorr, A. Lieb, S. Rath, M. Hanfland, B. Winkler, W. Schnick, High-pressure phase transition of the oxonitridosilicate chloride $Ce_4[Si_4O_{3+x}N_{7-x}]Cl_{1-x}O_x$ with $x = 0.12$ and 0.18, Z. Kristallogr. 220 (2005) 245–249.
[27] O.L. Anderson, J.E. Nafe, The bulk modulus-volume relationship for oxide compounds and related geophysical problems, J. Geophys. Res. 70 (1965) 153–165.
[28] R.D. Shannon, Revised effective ionic radii and systematic studies of interatomic distances in halides and chalcogenides, Acta Crystallogr. Sect. A Found. Crystallogr. 32 (1976) 751–767.
[29] R.K. Verma, Elasticity of some high-density crystals, J. Geophys. Res. 65 (1960) 757–766.
[30] M.T. Vaughan, D.J. Weidner, The relationship of elasticity and crystal structure in andalusite and sillimanite, Phys. Chem. Miner. 3 (1978) 133–144.
[31] J.D. Bass, Elasticity of minerals, glasses and melts, in: T.J. Ahrens (Ed.), AGU Reference Shelf 2, Mineral Physics and Crystallography, A Handbook of Physical Constants, American Geophysical Union, 1995, pp. 45–63.
[32] H. Yang, R.M. Hazen, L.W. Finger, C.T. Prewitt, R.T. Downs, Compressibility and crystal structure of sillimanite, Al_2SiO_5, Phys. Chem. Miner. 25 (1997) 39–47.
[33] A. Friedrich, M. Kunz, B. Winkler, T. Le Bihan, High-pressure behavior of sillimanite and kyanite: compressibility, decomposition and indications of a new high-pressure phase, Z. Kristallogr. 219 (2004) 324–329.
[34] D. Balzar, H. Ledbetter, Crystal structure and compressibility of 3:2 mullite, Am. Mineral. 78 (1993) 1192–1196.
[35] W.M. Kriven, J.W. Palko, S. Sinogeikin, J.D. Bass, A. Sayir, G. Brunauer, H. Boysen, F. Frey, J. Schneider, High temperature single crystal properties of mullite, J. Eur. Ceram. Soc. 19 (1999) 2529–2571.
[36] B. Hildmann, H. Ledbetter, S. Kim, H. Schneider, Structural control of elastic constants of mullite in comparison to sillimanite, J. Am. Ceram. Soc. 84 (2001) 2409–2414.
[37] J.W. Palko, A. Sayir, S.V. Sinogeikin, W.M. Kriven, J.D. Bass, Complete elastic tensor for mullite ($\sim 2.5Al_2O_3 \cdot SiO_2$) to high temperatures measured from textured fibers, J. Am. Ceram. Soc. 85 (2002) 2005–2012.
[38] J. Schreuer, B. Hildmann, H. Schneider, Elastic properties of mullite single crystals up to 1400 °C, J. Am. Ceram. Soc. 89 (2006) 1624–1631.
[39] S. Haussühl, L. BohatLý, P. Becker, Piezoelectric and elastic properties of the nonlinear optical material bismuth triborate, BiB_3O_6, Appl. Phys. A Mater. Sci. Process. 82 (2006) 495–502.
[40] H.T. Stokes, D.M. Hatch, Isotropy Subgroups of the 230 Crystallographic Space Groups, World Scientific, Singapore, 1988.
[41] A. Neuhaus, Synthese, Strukturverhalten und Valenzzustände der anorganischen Materie im Bereich hoher und höchster Drücke, Chimia 18 (1964) 93–103.
[42] W. Kleber, K.-T. Wilke, Synthese und Kristallchemie anorganischer Stoffe bei hohen Drücken und Temperaturen, Cryst. Res. Technol. 4 (1969) 165–199.